

## **Supplementary Information for Publication**

# **Bi-containing n-FeWO<sub>4</sub> Thin Films Provide the Largest Photovoltage and Highest Stability for a sub-2 eV Band Gap Photoanode**

*Lan Zhou,<sup>a,1</sup> Aniketa Shinde,<sup>a,1</sup> Santosh K. Suram,<sup>a,2</sup> Helge S. Stein,<sup>a</sup> Sage R. Bauers,<sup>b</sup> Andriy Zakutayev,<sup>b</sup> Joseph S. DuChene,<sup>a,c</sup> Guiji Liu,<sup>d</sup> Elizabeth A. Peterson,<sup>d,e</sup> Jeffrey B. Neaton,<sup>d,e,f</sup> John M. Gregoire<sup>a,\*</sup>*

<sup>a</sup> Joint Center for Artificial Photosynthesis, California Institute of Technology; Pasadena, California 91125, United States; <sup>b</sup> Materials Science Center, National Renewable Energy Laboratory, Golden, Colorado 80401, United States; <sup>c</sup> Thomas J. Watson Laboratory of Applied Physics, California Institute of Technology; Pasadena, California 91125, United States; <sup>d</sup> Joint Center for Artificial Photosynthesis, Lawrence Berkeley National Laboratory, Berkeley, CA 94720, United States; <sup>e</sup> Department of Physics, University of California, Berkeley, Berkeley, CA 94720, United States; <sup>f</sup> Molecular Foundry, Lawrence Berkeley National Laboratory, Berkeley, CA 94720, United States; Kavli Energy NanoSciences Institute, University of California, Berkeley, Berkeley, CA 94720, United States.

## **Corresponding Author**

*\*gregoire@caltech.edu*

<sup>1</sup> Equal contribution.

<sup>2</sup> current address: Toyota Research Institute, Los Altos, CA 94022 United States.

## Methods

### 1. High-throughput synthesis and characterization

#### 1.1 PVD library synthesis

The Bi-W-Fe ternary and W-Fe binary composition libraries were synthesized atop a 100-mm-diameter either glass substrate with SnO<sub>2</sub>:F conducting layer (Tec-15) or Si wafer with thermal SiO<sub>2</sub> layer by co-sputtering of metal targets using radio-frequency (RF) power supplies in a custom-designed combinatorial sputtering system,<sup>1</sup> and post-deposition annealed at 610 °C for 1 hour. A summary table of 6 composition libraries with synthesis conditions is provided in Table S1. The Bi-W-Fe and W-Fe libraries were deposited as metals in Ar gas of 0.8 Pa with 10<sup>-5</sup> Pa base pressure and were followed by a post-deposition anneal in a box oven at 610 °C in air for 1 hour. The W-Fe\* library was duplicated on a SiO<sub>2</sub>/Si substrate for temperature-dependent resistivity measurement. The Bi-W-Fe\* and W-Fe\*\*\* libraries were deposited as oxides using 10% O<sub>2</sub> in the sputter atmosphere and subsequently annealed in air at 610 °C for 1 hour. The W-Fe\*\* library was fabricated via reactive sputtering using 1% O<sub>2</sub> in sputtering atmosphere, then annealed in an inert Ar atmosphere at 610 °C for 1 hour.

#### 1.2 Powder x-ray diffraction (XRD)

XRD was used to determine the crystal structures and phase distribution of composition libraries. XRD was performed using a Bruker DISCOVER D8 diffractometer with Cu K $\alpha$  radiation from a Bruker I $\mu$ S source. Diffraction images were collected using a two-dimensional VÅNTAC-500 detector and integrated into one-dimensional patterns using DIFFRAC.SUITE™ EVA software.

#### 1.3. X-ray fluorescence (XRF)

XRF measurements were performed to determine the library composition using an EDAX Orbis Micro-XRF system with an x-ray beam approximately 2 mm in diameter. The sensitivity factor for each element was calibrated using commercial XRF calibration standards (MicromatterTM). XRF was performed on a 2 mm spacing of 1521 positions on the composition libraries.

#### 1.4. Optical properties

Optical properties were characterized using a custom-built on-the-fly scanning ultraviolet-visible dual-sphere spectrometer to record transmittance and total reflectance simultaneously.<sup>2</sup> The band gap energies were estimated by automatic Tauc analysis.<sup>3</sup> The optical spectra were acquired on a 2-mm-grid of 1521 positions on the composition library.

### 1.5. Scanning droplet cell (SDC) photoelectrochemistry measurements

Our previously reported fiber-coupled SDC instrumentation was used to measure photoelectrochemical activity.<sup>4</sup> Experiments included a variety of O<sub>2</sub>-saturated electrolytes at four pH values (1, 3, 7, and 9) and LED illumination with four different wavelengths. The various electrolytes used are summarized in Table S5. Initial experiments across composition libraries measured four sequential chronoamperometry (CA) measurements at 1.23 V versus RHE with four LEDs toggled with 0.5 s on, 0.5 off illumination:  $3.2 \pm 0.05$  eV for 15 s; and  $2.74 \pm 0.09$ ,  $2.4 \pm 0.09$ , and  $2.07 \pm 0.03$  eV all for 4 s each (Tables S3 and S4). Lastly, cyclic voltammetry (CV) was performed with 3.2 eV illumination with light toggling 2 s on, 1 s off, and a voltage range of 1.23 to 0.73 to 1.53 V versus RHE (rate of  $0.02$  V s<sup>-1</sup>). SDC was rastered along the composition library and performed this sequence of experiments every 5.5 mm on the ternary library (215 positions), and every 3 mm along one line of the binary library (29 positions). External quantum efficiency (EQE) was calculated using photocurrent measured at 1.23 V vs RHE at each illumination energy and an illumination area of 0.0113 cm<sup>2</sup>. Photoelectrochemical stability was characterized by 30 mins chopped-illumination (10 s on, 5 s off) photocurrent measurements at 1.23 eV vs RHE on select samples with 2.4 eV illumination in various electrolytes.

The longer stability measurements of Figure 4 include 34 repetitions of the ~100 s CV and ~50 min CA. Between each repetition, the electrochemical cell was removed for about 2 minutes for maintenance (flushing solution through the fritless Ag/AgCl microelectrode to maintain a stale reference potential). For days 6 and 7 this time of air exposure was increased to 30 min, providing an increase in the subsequent photocurrent compared to repeated CV+CA measurements on previous days. The sample was kept in ambient air for approximately 18 hours between days of testing, except for after day 4 where approximately 70 hours elapsed between measurements including exposure to vacuum for the XRF measurement, and after day 6 where approximately 40 hours elapsed between measurements, which corresponds to a total span of 10 calendar days for the 7 days of PEC testing. After overnight air exposure the initial photocurrent, and after multiple-day air exposure the decay in the photocurrent is also more gradual. The signals from the 3rd CA of day 4 and the 3rd CA of day 6 show variability that is believed to originate from an issue with the PEC cell, in particular with light transmission and reference electrode potential variation, respectively.

## 2. Traditional characterization

## 2.1 AM 1.5 photoelectrochemistry measurements

The sample of interest was cut out from the Bi-W-Fe ternary library to make an epoxy-encapsulated electrode which was characterized in a traditional, single-compartment, three-electrode electrochemical cell with a potentiostat (Bio-Logic, SP-300) under simulated AM 1.5G solar light irradiation ( $100 \text{ mW cm}^{-2}$ , 16S-300-002, Solar Light). The fabricated electrode, a platinum wire, and Ag/AgCl electrode were used as working, counter, and reference electrodes, respectively. Cyclic voltammograms were performed first in the dark then under continuous front-side illumination at a sweep rate of  $0.05 \text{ V s}^{-1}$ .

## 2.2. Electrochemical impedance spectroscopy (EIS) and Mott-Schottky analysis

was performed on a  $0.48 \text{ cm}^2$  region of the film containing primarily FeWO<sub>4</sub> in a three-electrode configuration with FeWO<sub>4</sub> as the working electrode, a Pt wire mesh counter electrode, and a Ag/AgCl reference electrode all immersed in the same electrolyte as PEC measurements, pH 9 borate buffer with 0.01 M sodium sulfite. The electrolyte was sparged with N<sub>2</sub> gas prior to measurements to remove dissolved O<sub>2</sub> from the solution and experiments were conducted under a N<sub>2</sub> blanket. The impedance was determined by applying a sinusoidal voltage (20 mV amplitude) to the working electrode at a range of frequencies (0.1–50 kHz) across a range of applied potentials. All impedance measurements were performed under dark conditions. The carrier concentration and conductivity type (n-type or p-type) of the working electrode was obtained by Mott-Schottky analysis of the data obtained at higher frequencies (1-10 kHz), where it is known that the system can be reasonably represented by a resistor in series with a capacitor.<sup>5</sup> A dielectric constant of 18.95 was used for the FeWO<sub>4</sub> phase.<sup>6</sup>

## 2.3. X-ray photoelectron spectroscopy (XPS)

XPS spectra were measured on selected samples to determine the near-surface chemistry using a Kratos Axis NOVA with excitation from a monochromatized Al K $\alpha$  radiation at 300 W (20 mA at 15 kV). The collected spectra were calibrated to the carbon 1s peak of 284.8 eV.

## 2.4. Cross-section scanning electron microscopy (SEM)

The Bi-W-Fe ternary library was cleaved and the area near sample A was chosen for cross-section SEM imaging in a FEI Nova NanoSEM 450 using a 15 kV electron beam to measure the film thickness.

## 2.5. Temperature-dependent resistivity measurements (on sample from W-Fe\* binary library)

were collected using the van der Pauw method on a Lakeshore 8425 probe station equipped with a closed-cycle He cryostat. Indium contacts were pressed onto the sample and Ohmic IV

curves were observed at each temperature. Measurements were made with a voltage compliance of 10 V and maximum current of 10  $\mu$ A.

2.6. Room-temperature Seebeck coefficient measurements (on sample from W-Fe\* binary library) were collected on a house-built system. The sample was suspended between two Cu blocks using Indium dots as contacts and heaters installed in each block were used to create a slight temperature difference (ca. 1, 2, -1, -2 K) across them. After a stabilization period of five minutes, voltages were measured at each side. The Seebeck coefficient determined from the slope of the  $V/\Delta T$  curve was then corrected to account for the known Seebeck voltages of the system.

### 3. Computational Methods

#### 3.1 Electronic structure calculations

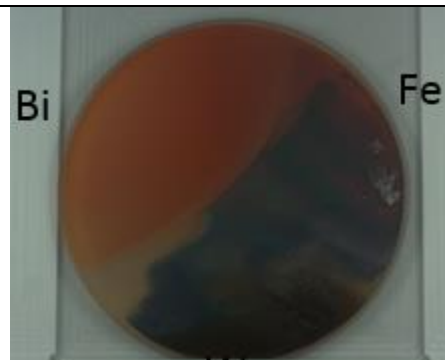
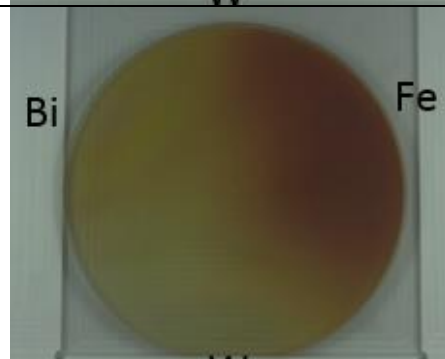
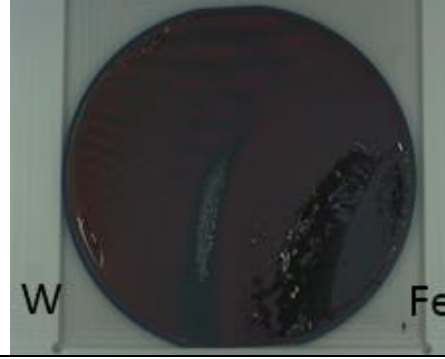
First-principles calculations are performed using density functional theory (DFT) with a plane-wave basis and projector augmented wave (PAW) potentials<sup>7</sup> as implemented by the Vienna *ab-initio* simulation package (VASP).<sup>8</sup> All calculations are spin-polarized and performed in the generalized gradient approximation as implemented by Perdew, Burke and Ernzerhof (PBE),<sup>9</sup> with the addition of a Hubbard U term (GGA+U)<sup>10</sup> to account for on-site localization on the Fe and W ions. U values of 5.3 and 6.2 were used for Fe and W respectively.<sup>11</sup> A plane-wave energy cut-off of 500 eV was used with a  $5\times 4\times 4$  Gamma-centered k-point mesh. Structural relaxations are performed in all cases until forces and stress tensor values are less than 0.001 eV/ $\text{\AA}$ . Tables S6 lists the optimized lattice parameters for comparision with experimental values. Band structures are generated for both ferromagnetic (FM) and antiferromagnetic (AFM) spin configurations of the Fe atoms.

#### 3.2 Phase energetics calculations

The phase diagram is generated with the Materials Project<sup>12</sup> using the pymatgen<sup>13</sup> Grand Potential Phase Diagram function with fixed values of the chemical potentials of O<sub>2</sub> corresponding to partial pressures of O<sub>2</sub> ranging from 1.0 atm to 1e-8 atm at a fixed temperature of 883K (the annealing temperature from experiments). Above hull energies are calculated with respect to the most stable species in the entire Fe-W phase space at the selected partial pressure of O<sub>2</sub>. In cases where the Materials Project has multiple entries for a given chemical formula, only the most stable entry is displayed. Note that the energies above hull for Fe<sub>2</sub>O<sub>3</sub> and WO<sub>3</sub> are the same throughout the displayed regions of the phase diagram.

Chemical potential of O<sub>2</sub> is calculated semi-empirically according to formula (2) from Ong et al.,<sup>14</sup> modified to use formation energies per atom in agreement with the pymatgen Grand Potential function. Formation energies of each chemical species are taken from the Materials Project DFT results and the temperature-dependent entropy of O<sub>2</sub> used in the chemical potential calculations are taken from NIST reference values (<https://janaf.nist.gov/tables/O-029.html>).

Table S1. Summary of 6 composition libraries with their synthesis conditions and post thermal annealing photos. The \* denote different versions of the library and these library labels are used in this ESI text.

<b>Library</b>	<b>Substrate</b>	<b>Deposition</b>	<b>Annealing</b>	<b>Photo</b>
Bi-W-Fe	FTO-coated Pyrex Tec15 glass	metal, Ar (6mTorr)	air, 610°C,1hr	
Bi-W-Fe*	FTO-coated Pyrex Tec15 glass	oxide, O <sub>2</sub> /Ar (0.6/5.4 mTorr)	air, 610°C,1hr	
W-Fe	FTO-coated Tec15 glass	metal, Ar (6mTorr)	air, 610°C,1hr	
W-Fe*	SiO <sub>2</sub> /Si wafer	metal, Ar (6mTorr)	air, 610°C,1hr	

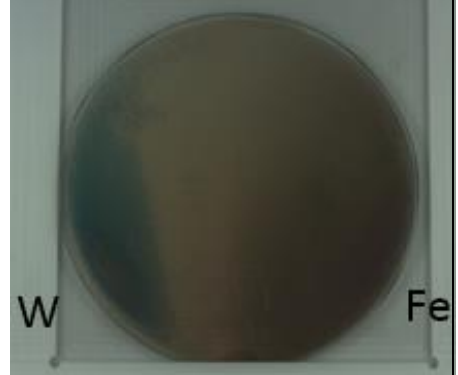
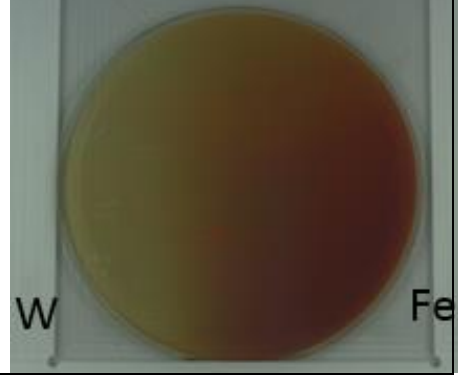
W-Fe**	FTO-coated Tec15 glass	oxide, O <sub>2</sub> /Ar (0.06/5.94 mTorr)	Ar, 610°C,1hr	
W-Fe***	FTO-coated Tec15 glass	oxide, O <sub>2</sub> /Ar (0.6/5.4 mTorr)	air, 610°C,1hr	

Table S2. Summary of 5 samples in the main text with corresponding composition and phase information.

Sample	Library	Composition	XRD	Figures
A	Bi-W-Fe	Fe <sub>0.56</sub> W <sub>0.38</sub> Bi <sub>0.06</sub> O <sub>z</sub>	FeWO <sub>4</sub> + Bi <sub>2</sub> O <sub>3</sub>	Fig.1, Fig.2, Fig.3
B	Bi-W-Fe	Fe <sub>0.54</sub> W <sub>0.35</sub> Bi <sub>0.11</sub> O <sub>z</sub>	FeWO <sub>4</sub> + Bi <sub>2</sub> O <sub>3</sub>	Fig.1
C	Bi-W-Fe	Fe <sub>0.59</sub> W <sub>0.35</sub> Bi <sub>0.06</sub> O <sub>z</sub>	FeWO <sub>4</sub> + Bi <sub>2</sub> O <sub>3</sub>	Fig.1
D	W-Fe	Fe <sub>0.62</sub> W <sub>0.38</sub> O <sub>z</sub>	FeWO <sub>4</sub> + Fe <sub>2</sub> O <sub>3</sub>	Fig.5
E	Bi-W-Fe	Fe <sub>0.59</sub> W <sub>0.36</sub> Bi <sub>0.05</sub> O <sub>z</sub>	FeWO <sub>4</sub> + Bi <sub>2</sub> O <sub>3</sub>	Fig.4

Table S3. Irradiance for scanning droplet cell experiments in Figures 1 and 2 in main text.

LED (eV) (Doric LEDC4)	Irrad. mW cm <sup>-2</sup> , base pH
3.2 ± 0.05	369
2.74 ± 0.09	328
2.4 ± 0.09	136
2.07 ± 0.03	86

Table S4. Irradiance for scanning droplet cell experiments in Figures 3 and 4 in main text.

LED eV (Doric LEDC4)	Irrad. mW cm <sup>-2</sup> , neutral/base pH	Irrad. mW cm <sup>-2</sup> , acid pH
3.2 ± 0.05	249	152
2.74 ± 0.09	223	114
2.4 ± 0.09	87	49
2.07 ± 0.03	60	34

Table S5. Summary of electrolytes used in PEC measurements.

pH	Abbreviation	Electrolyte + (sacrificial hole acceptor)
1.4	MET1.4	0.1 M sulfuric acid + 0.25 sodium sulfate + (0.1 M methanol)
3	OER3	0.1 M potassium phosphate monobasic + 0.04 phosphoric acid + 0.25 sodium sulfate
3	MET3	0.1 M potassium phosphate monobasic + 0.04 phosphoric acid + 0.25 sodium sulfate + (0.1 M methanol)
6.6	SLF6.6	0.05 potassium phosphate monobasic + 0.05 potassium phosphate dibasic + 0.25 M sodium sulfate + (0.01 M sodium sulfite)
9	OER9	0.1 boric acid + 0.05 potassium hydroxide + 0.25 M sodium sulfate
9	SLF9	0.1 boric acid + 0.05 potassium hydroxide + 0.25 M sodium sulfate + (0.01 M sodium sulfite)

### Additional PEC characterization of Bi-Fe-W oxides

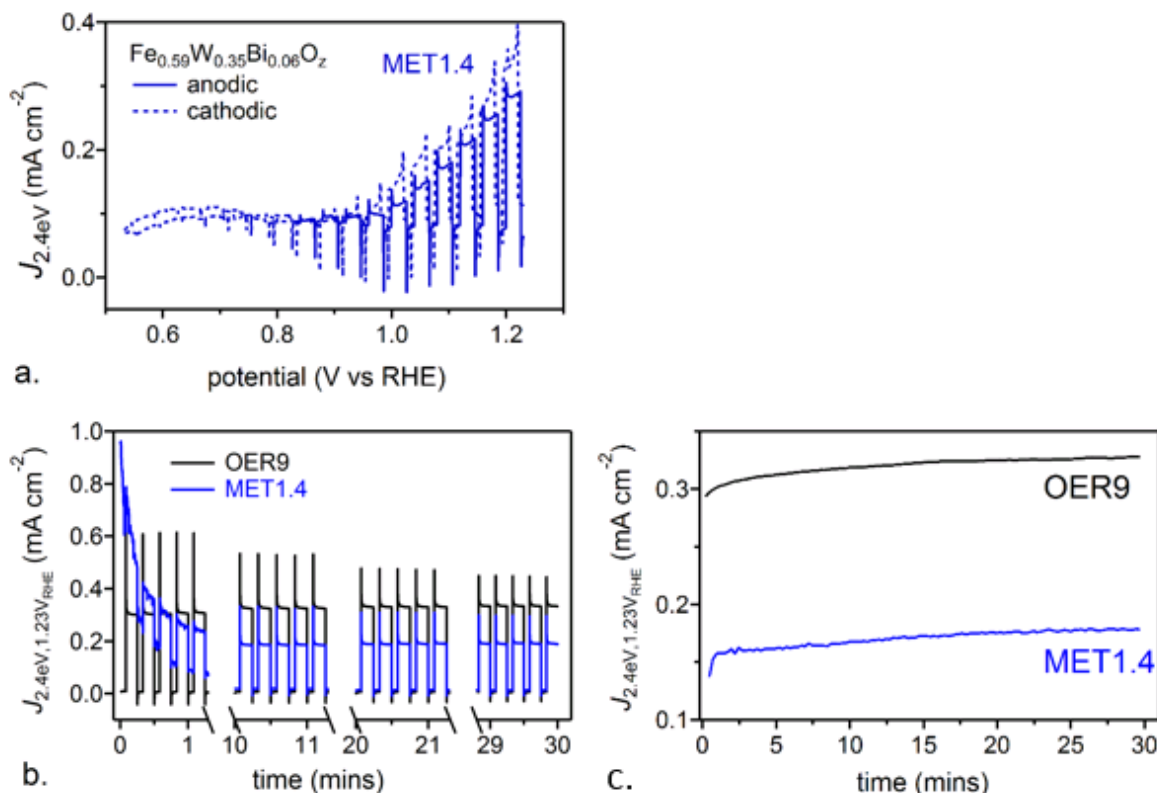


Figure S1. (a) Front-side toggled-illumination (2.4 eV LED) cyclic voltammograms (CV) of sample C ( $\text{Fe}_{0.59}\text{W}_{0.35}\text{Bi}_{0.06}\text{O}_z$ ) starting with a cathodic sweep from 1.23 eV vs RHE (dashed line) and finishing with an anodic sweep back to 1.23 eV vs RHE in aqueous pH 1.4 electrolyte with 0.1 M methanol (MET1.4). PEC stability as characterized by 30 min toggled 2.4 eV illumination at 1.23 eV vs RHE in OER9 and MET1.4 electrolytes, with representative illumination cycles shown in (b) and the photocurrent density shown in (c).

PEC data on sample B ( $\text{Fe}_{0.54}\text{W}_{0.35}\text{Bi}_{0.11}\text{O}_z$ ) in Bi-W-Fe ternary library. The XRD shows the presence of  $\text{FeWO}_4$  with the minority phase monoclinic  $\text{Bi}_2\text{O}_3$ .

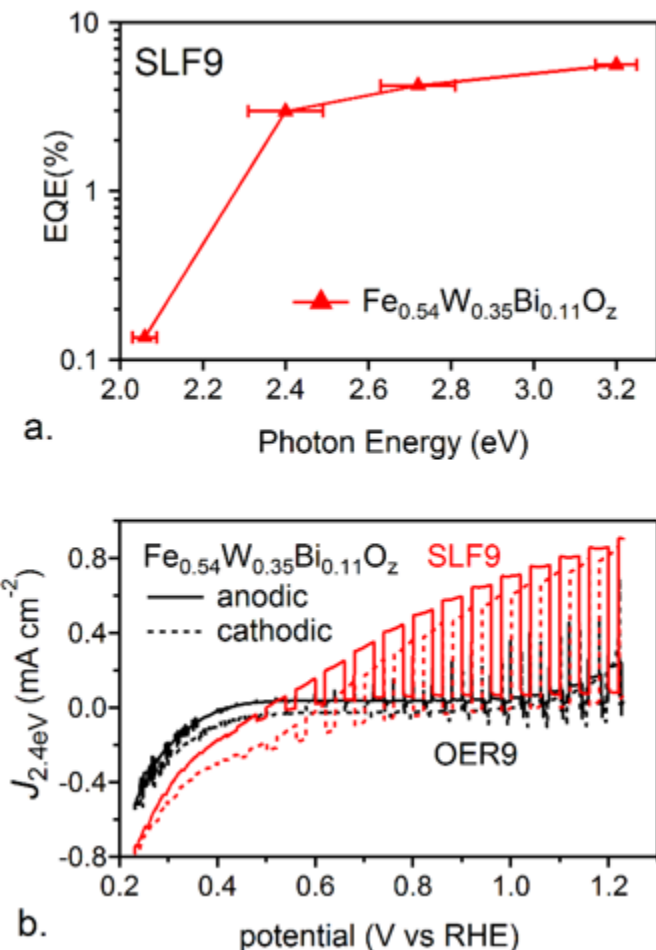


Figure S2. (a) The spectral external quantum efficiency (EQE) of sample B ( $\text{Fe}_{0.54}\text{W}_{0.35}\text{Bi}_{0.11}\text{O}_z$ ) in aqueous pH 9 borate electrolyte with 0.01 M sodium sulfite (SLF9) electrolyte for 4 different LEDs (2.07, 2.4, 2.74, and 3.2 eV). (b) Front-side toggled-illumination (2.4 eV LED, 2 s on and 1 s off) cyclic voltammograms (CV) of this sample starting with a cathodic sweep from 1.23 eV vs RHE (dashed line) and finishing with an anodic sweep back to 1.23 eV vs RHE in aqueous pH 9 borate electrolyte with (SLF9, red) and without (OER9, black) sodium sulfite.

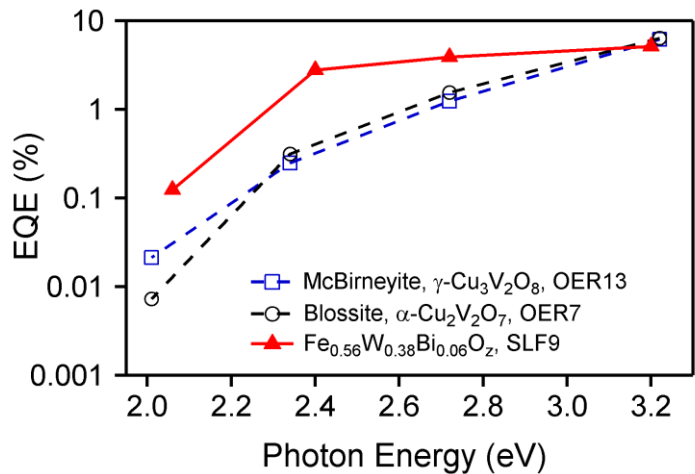


Figure S3. Spectral external quantum efficiency (EQE) of  $\text{Fe}_{0.56}\text{W}_{0.38}\text{Bi}_{0.06}\text{O}_z$  in SLF9 electrolyte, along with the EQE of previously published<sup>15</sup> McBirneyite ( $\gamma\text{-Cu}_3\text{V}_2\text{O}_8$ ) in OER13 and Blossite ( $\alpha\text{-Cu}_2\text{V}_2\text{O}_7$ ) in OER7 electrolyte. The  $\text{Fe}_{0.56}\text{W}_{0.38}\text{Bi}_{0.06}\text{O}_z$  consistently outperforms the copper vanadates at photon energies below 2.7 eV: by a factor of 3 at 2.7 eV and a factor of 10 at 2.4 eV.

## XRD characterization

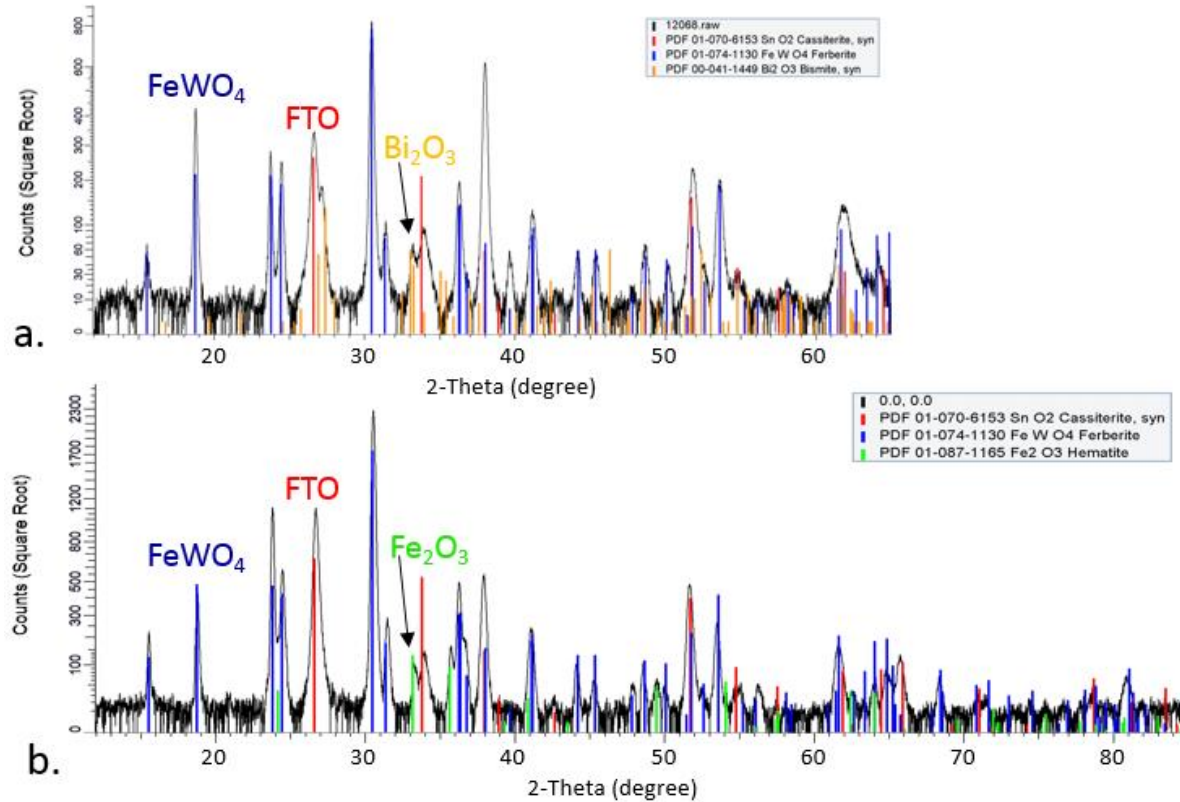


Figure S4. Integrated 1D XRD patterns of (a) sample A ( $\text{Fe}_{0.56}\text{W}_{0.38}\text{Bi}_{0.06}\text{O}_z$ ) in Bi-W-Fe ternary oxide library and (b) sample D ( $\text{Fe}_{0.62}\text{W}_{0.38}\text{O}_z$ ) in the W-Fe binary oxide library, respectively. Besides the strong signals from FTO substrate layer (red sticks), both samples contain the majority phase of monoclinic  $\text{FeWO}_4$  (blue sticks) with space group of P2/c (ICDD: 01-074-1130), with minority phases monoclinic  $\text{Bi}_2\text{O}_3$  (orange) in the ternary (a) and rhombohedral  $\text{Fe}_2\text{O}_3$  (green) in the binary (b).

## XPS characterization

The chemical composition and surface chemical states of two Bi-W-Fe oxide samples (A and B) was investigated by XPS, and the corresponding spectra are shown in Figure S5. When quantifying XPS spectra, Relative sensitivity factors (RSF) are used to scale the measured peak areas so that variations in the peak areas are representative of the amount of materials in the sample surface. The following RSF is from the reference:

<http://www.xpsfitting.com/2009/04/relative-sensitivity-factors-rsf.html>

Fe 2p = 2.957; W 4f = 3.523; Bi 4f = 9.14

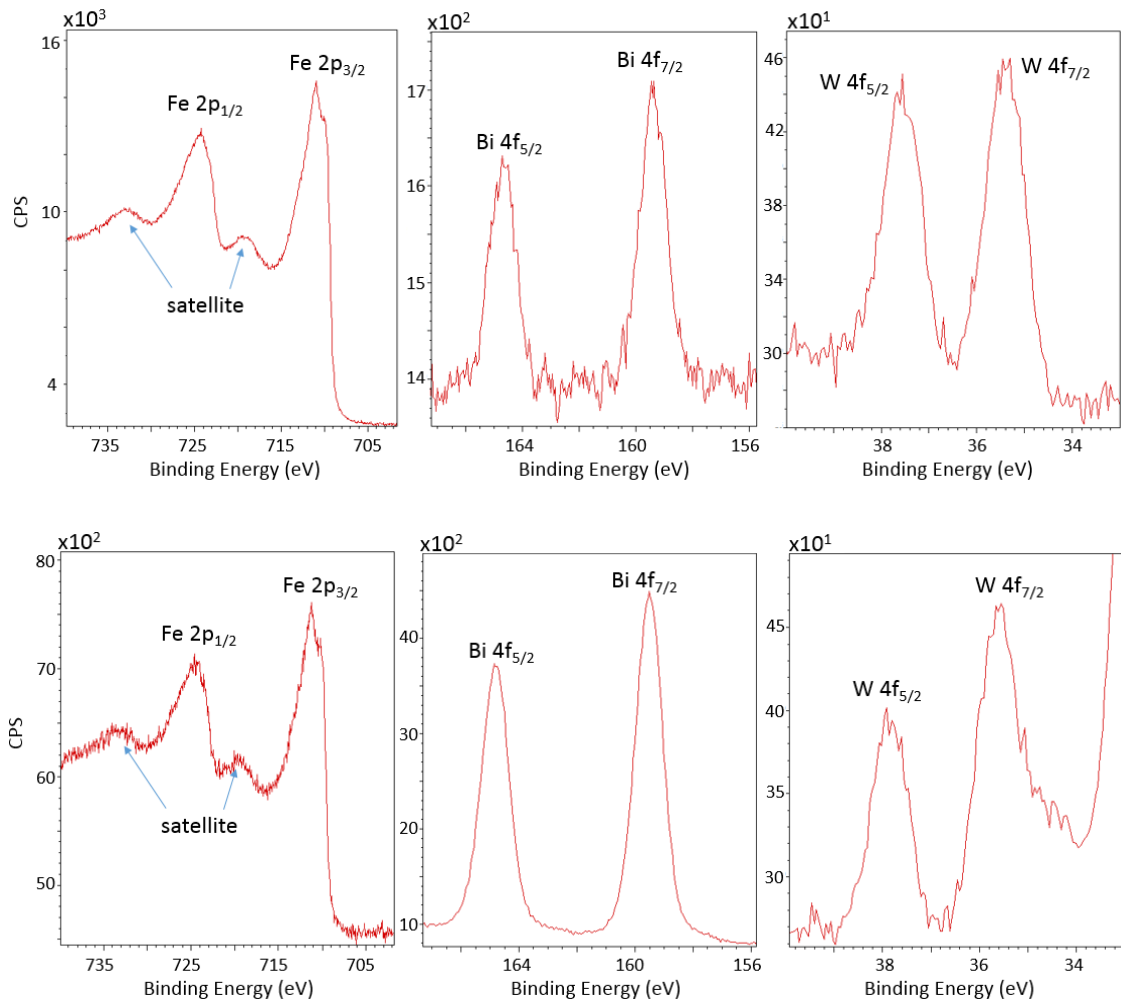


Figure S5. High resolution core-level XPS spectra of Fe 2p, Bi 4f, and W 4f of the sample A ( $\text{Fe}_{0.56}\text{W}_{0.38}\text{Bi}_{0.06}\text{O}_z$ , top panel) and sample B ( $\text{Fe}_{0.54}\text{W}_{0.35}\text{Bi}_{0.11}\text{O}_z$ , bottom panel) in Bi-W-Fe ternary oxide library post SDC measurements in Figure 1 of maintext. The binding energy was calibrated to C 1s peak position of 284.8 eV. Elemental quantification was performed in the CasaXPS software using a Shirley background fitting. The composition shows 99% Fe and less than 1% Bi and W on the film surface.

In both samples, the surface contents of  $\text{Fe}^{3+}$  species are dominant. Those  $\text{Fe}^{3+}$  species only exist on the surface of  $\text{FeWO}_4$  since no new iron compounds in the bulk were detected by XRD characterization.

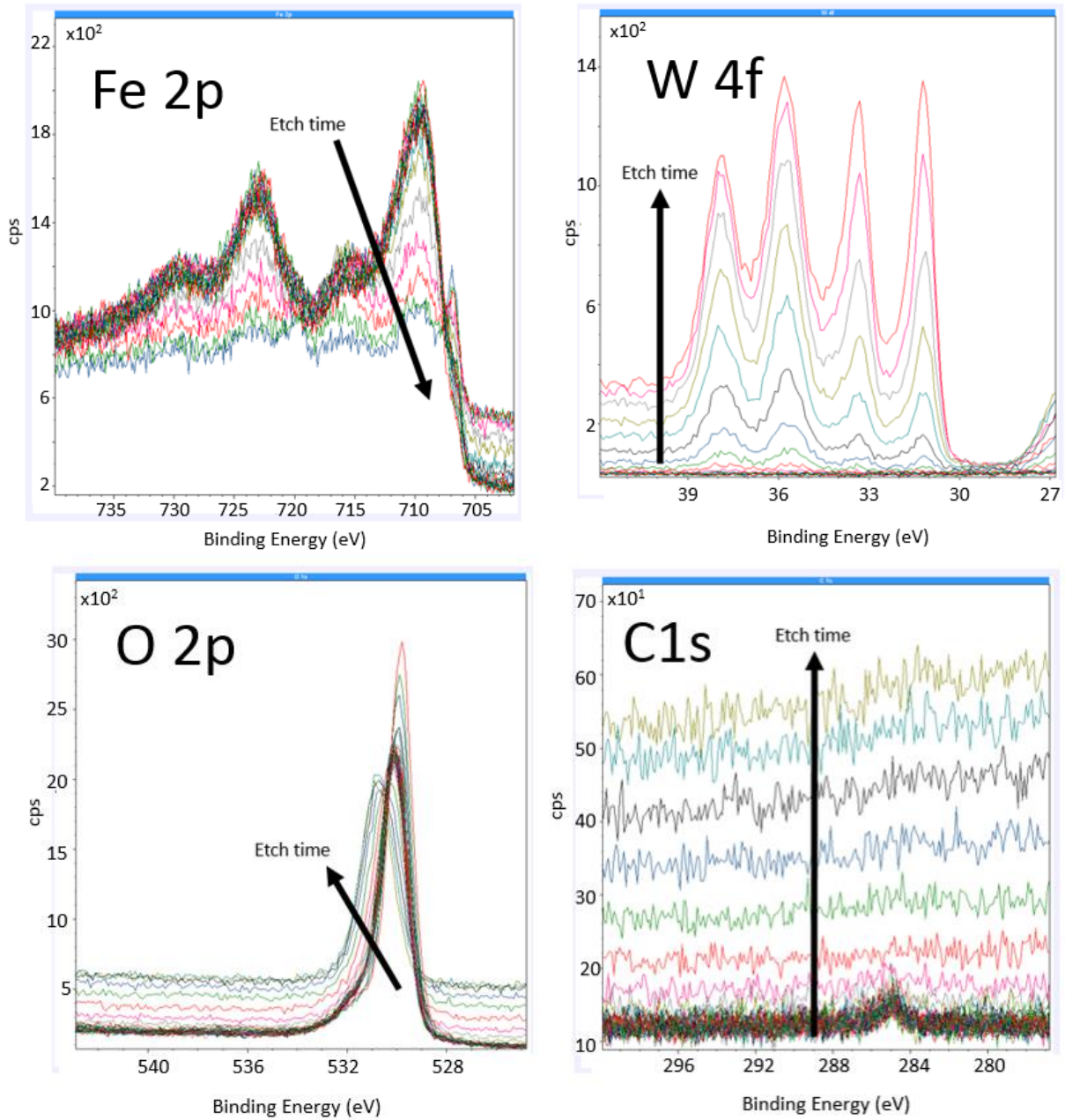


Figure S6. Depth-profile XPS: the high resolution core-level XPS spectra of Fe 2p, W 4f, O 2p and C 1s, respectively, as a function of etching time on the as-annealed film  $\text{Fe}_{0.62}\text{W}_{0.38}\text{O}_2$  in W-Fe binary oxide library. XRD pattern in Figure S4b indicates a phase mixture of  $\text{FeWO}_4$  and  $\text{Fe}_2\text{O}_3$ . Strong Fe 2p signal on the original surface (without etching) and the appearance of W 4f signal after certain etching period reveals that  $\text{Fe}_2\text{O}_3$  appears on top of film surface and  $\text{FeWO}_4$  is underneath the  $\text{Fe}_2\text{O}_3$  layer. Since the etching rate is not calibrated, the thickness of  $\text{Fe}_2\text{O}_3$  layer is not defined.

## Additional PEC characterization of Fe-W oxides

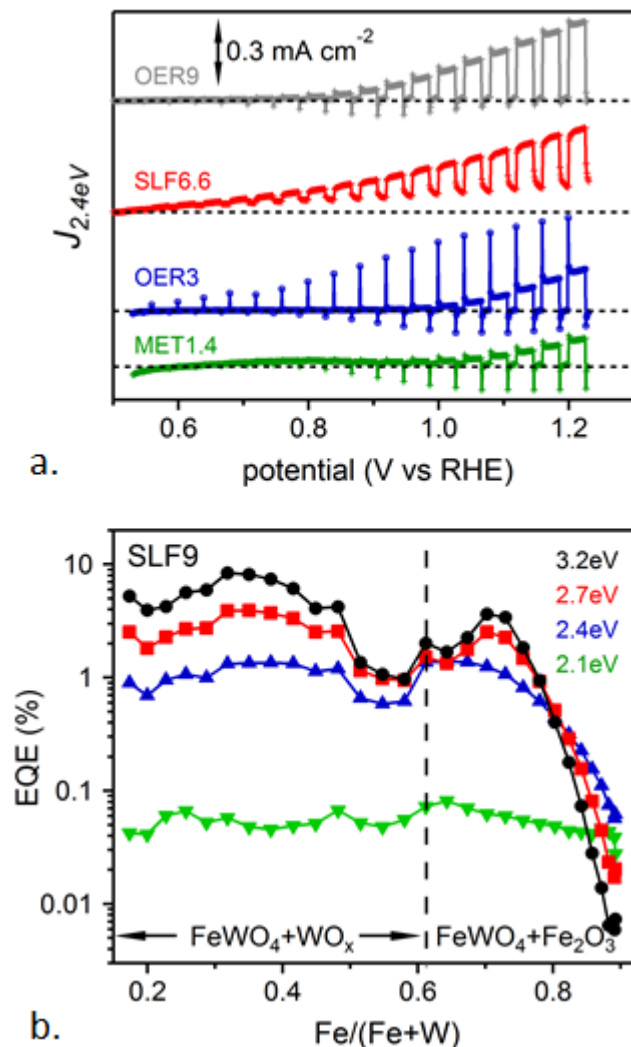


Figure S7. a) Anodic sweeps of 2.4 eV illumination CVs of sample  $\text{Fe}_{0.62}\text{W}_{0.38}\text{O}_z$  in various electrolytes. b) The EQE measured in SLF9 electrolyte under 4 different illuminations as a function of Fe content in the W-Fe binary composition library. The dashed line represents the sample with 62% of Fe containing phase mixture of 96%  $\text{FeWO}_4$  and 4%  $\text{Fe}_2\text{O}_3$ , and it separates the phase mixed regions of  $\text{FeWO}_4$  with tungsten oxides and  $\text{FeWO}_4$  with iron oxides.

## Electronic characterization of Fe-W oxides

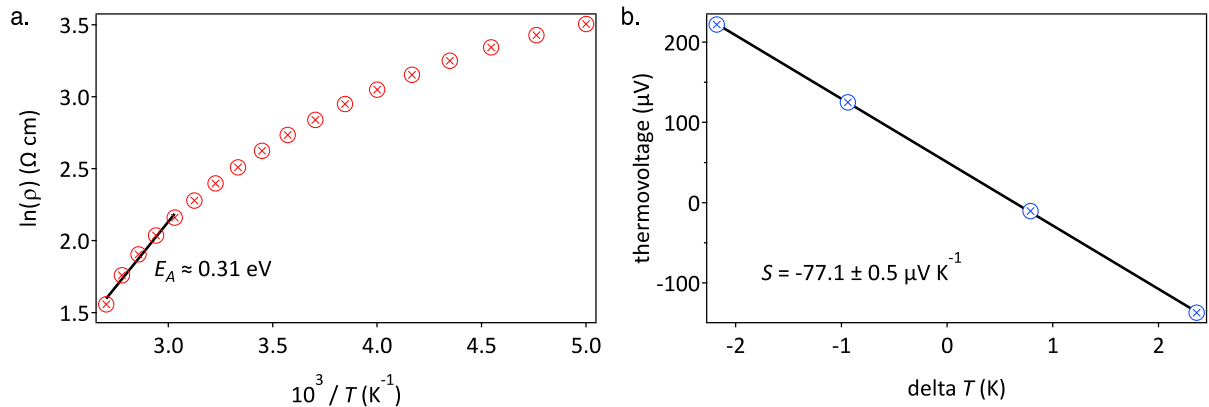


Figure S8. Electronic properties of  $\text{FeWO}_4$  (in W-Fe\* binary oxide library, deposited on  $\text{SiO}_2/\text{Si}$ ). (a) Temperature dependence of the resistivity of sample. XRD pattern indicates that the layer of  $\text{Fe}_2\text{O}_3$  formed on top of  $\text{FeWO}_4$  delaminated off of the film surface. Assuming a material mobility on the order of  $0.1 \text{ cm}^2 \text{ V}^{-1} \text{ s}^{-1}$ , the  $4 - 40 \Omega \text{ cm}$  resistivity suggests a carrier density on the order of  $10^{18}\text{-}10^{19} \text{ cm}^{-3}$ . The temperature-dependent resistivity shows that the film appears semiconducting though with a weaker than exponential turn-on. This suggests the film is not a purely ‘intrinsic’ behavior. The defect activation energy corresponding to the black line is about 0.31 eV but the data in this plot do not contain an extensive linear region. (b) According to the Seebeck measurements, the film is unambiguously n-type. The measured Seebeck coefficient is  $S = -77.1 \pm 0.5 \mu\text{V/K}$ , where  $0.5 \mu\text{V/K}$  is combination of known system uncertainty and fit error of the  $dV/dT$  line. The intermediate magnitude of the Seebeck value indicates that the sample is not degenerately doped (e.g.  $-10 \mu\text{V/K}$  for ITO), but that the doping is not too low either (usually a few  $100 \mu\text{V/K}$  for PV absorbers with  $\sim 1 \times 10^{16} \text{ cm}^{-3}$  carrier density).

## Computational characterization of FeWO<sub>4</sub>

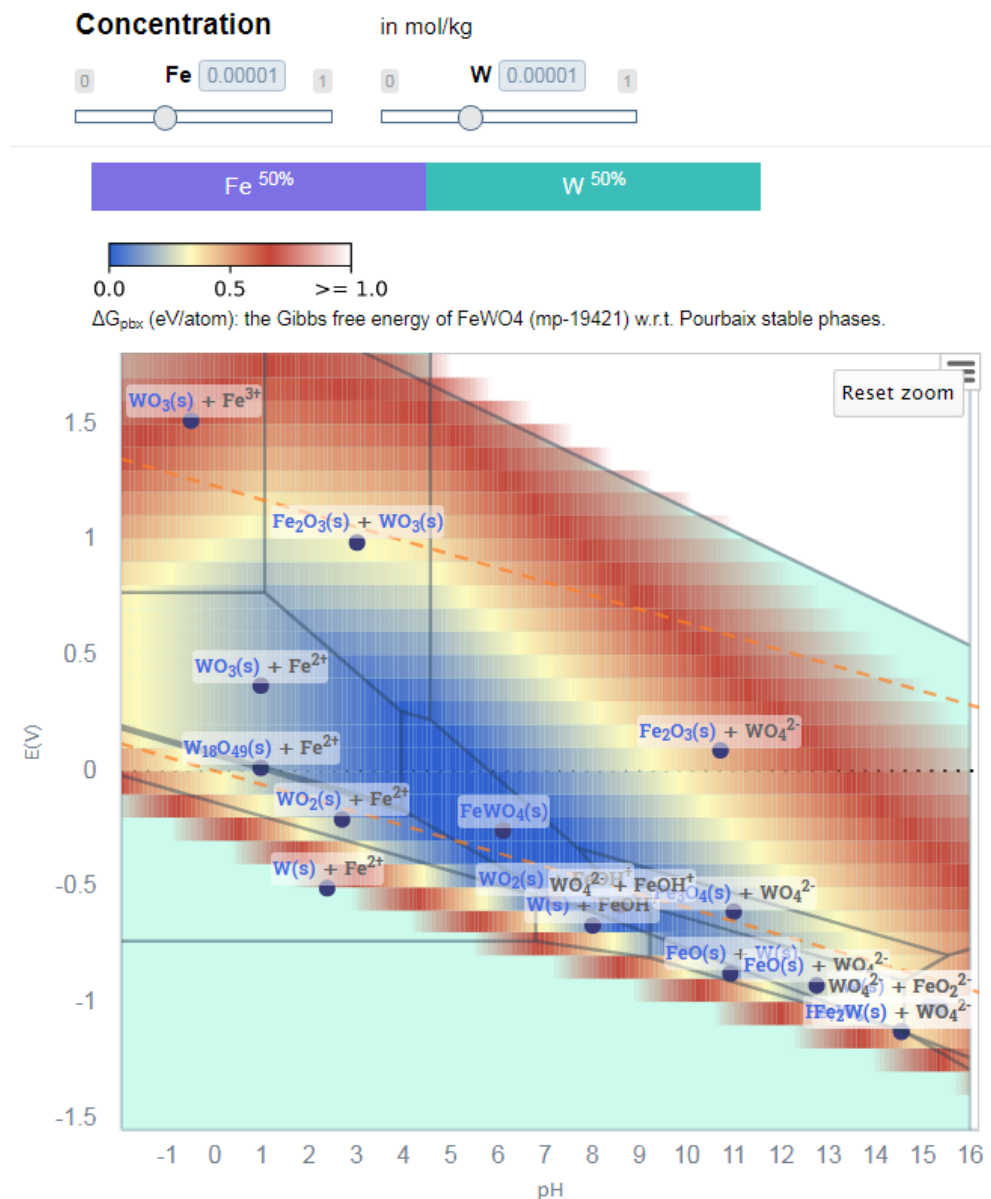


Figure S9. Pourbaix diagram of Fe-W-O system for 50:50 Fe:W from the Materials Project web application. The Gibbs free energy ( $\Delta G_{pbx}$ ) of the FeWO<sub>4</sub> with respect to the Pourbaix stable phases is superimposed on the Pourbaix diagram and represented by the color bar.

Table S6. DFT- GGA+U lattice parameters for FeWO<sub>4</sub> for both magnetic configurations along with experimental values. The lattice parameter *a* for the AFM configuration is taken as half the value of the 2×1×1 supercell.

	<i>a</i> (Å)	<i>b</i> (Å)	<i>c</i> (Å)
DFT, FM	4.787	5.820	5.080
DFT, AFM	4.804	5.790	5.094
ICSD ID 26843	4.730	5.703	4.952

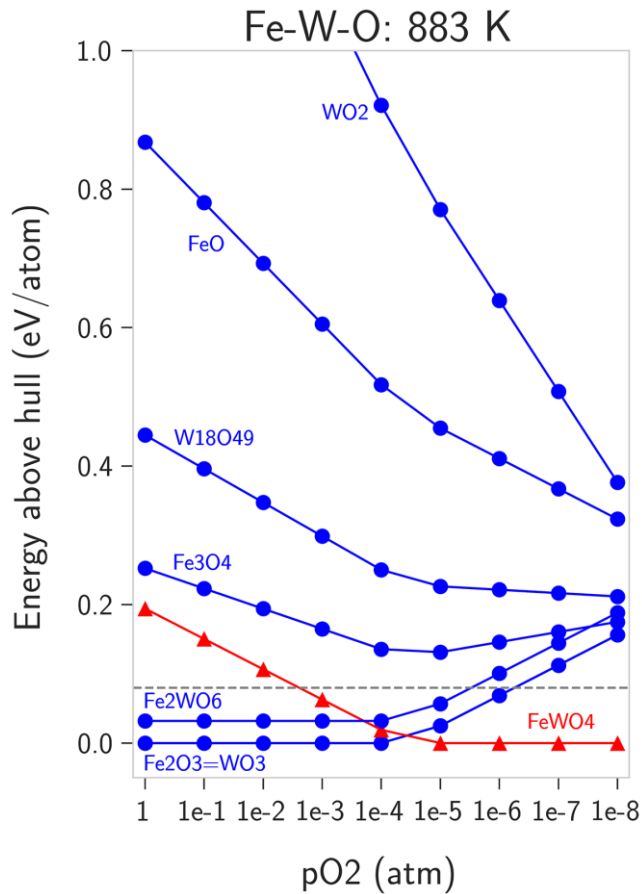


Figure S10. Above-hull energies for phases in the Fe-W-O system at 610 °C (883 K) at varying O<sub>2</sub> partial pressure. The lowest-energy polytype at each formula unit is shown, and the plotted energy for a given phase is the above hull energy at the respective Fe-W stoichiometry with chemical potential of oxygen determined by the partial pressure and temperature. The dashed line at 0.08 eV/atom indicates the nominal threshold corresponding to the typical maximum above-hull energy of experimentally-observed phases.

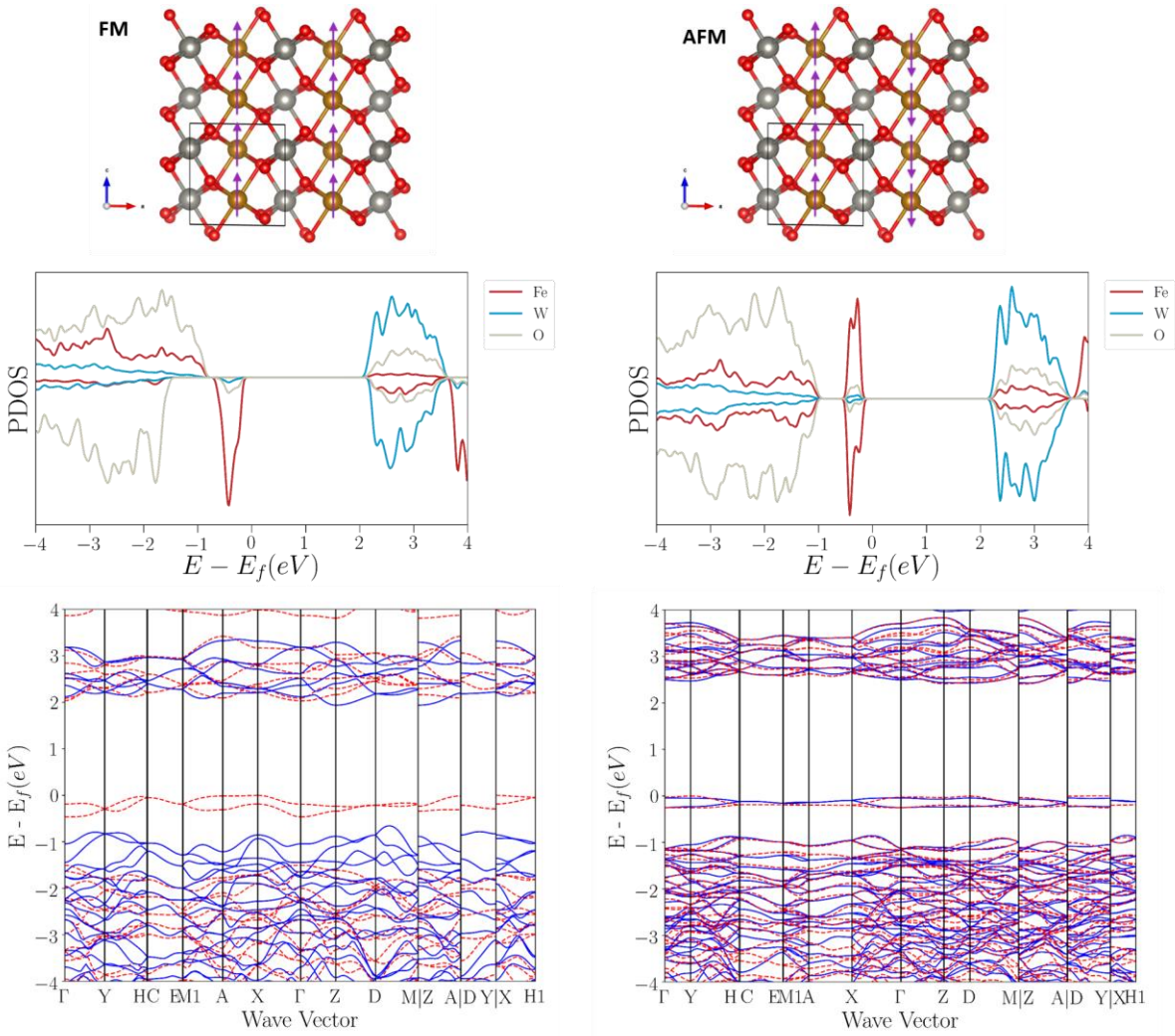


Figure S11. The spin configuration (top), PDOS (middle) and band structure (bottom, blue = spin up, red = spin down) for  $\text{FeWO}_4$  with 2 different magnetic configurations, FM (left) and AFM (right).

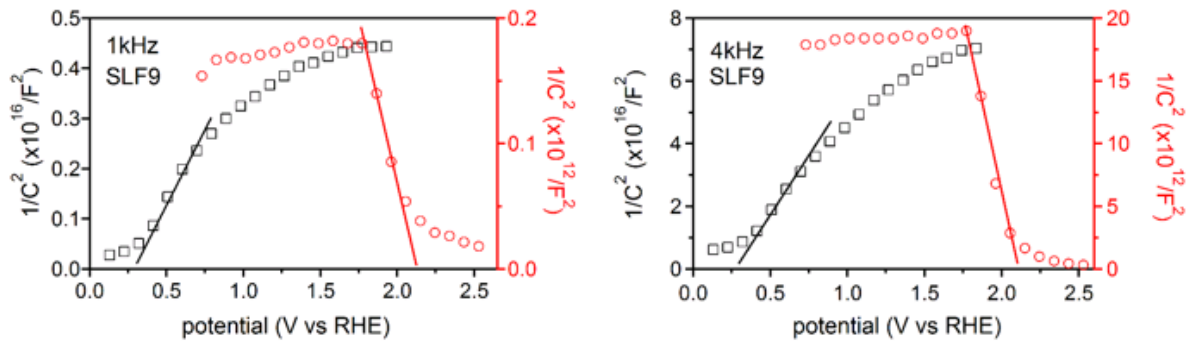


Figure S12. Mott-Schottky plots for two  $\text{FeWO}_4$  electrodes with different synthesis methods acquired in SLF9 electrolyte at 1 and 4 kHz, respectively.

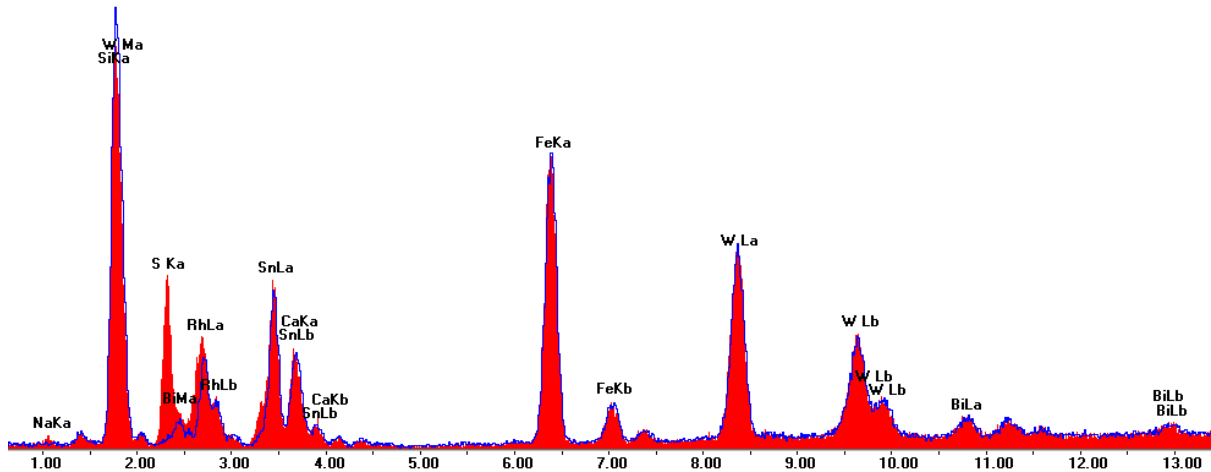


Figure S13. Wider range XRF spectra of Figure 4c for  $\text{Fe}_{0.59}\text{W}_{0.36}\text{Bi}_{0.05}\text{O}_z$  sample before (blue line) and after (filled, red color) photoelectrochemical measurement at the end of day4. Both spectra show Fe K, W L, and Bi L peaks used for composition quantification, as well as signals from the FTO layer (Sn), glass substrate (Si, Ca), and X-ray source (Rh). The post-photoelectrochemistry measurement spectrum also includes a signal S  $K_{\alpha}$  from the electrolyte salt, indicating that upon drying of the samples, some electrolyte salts precipitated on the sample surface.

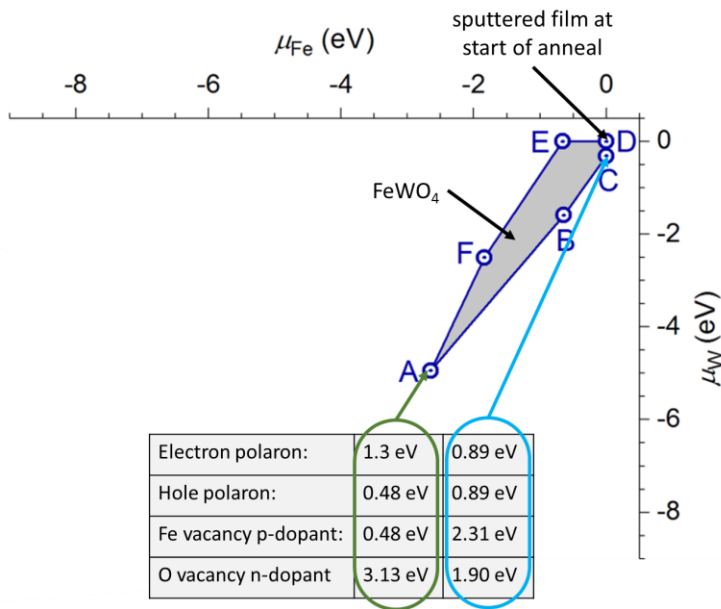


Figure S14. Analysis of defect energetics based on Hoang et al. Figure 3a (partially reproduced with permission from publisher).<sup>6</sup> The point defects and polarons with lowest formation energy at the respective chemical potential coordinates are tabulated in the figure. These formation energies, combined with the lower self-trapping energy and migration barrier of electron polarons compared to hole polarons (see Ref. <sup>6</sup>) predict p-type conductivity near point A and n-type conductivity near point C, which correspond to the low  $\mu_{\text{Fe}}$  and high  $\mu_{\text{Fe}}$  limits, respectively, of the  $\text{FeWO}_4$  stability region (shaded gray). The high Fe concentration in our  $\text{FeWO}_4$  synthesis indicates the high  $\mu_{\text{Fe}}$  region is more representative of our synthesis, and given that annealing started with the metal film that corresponds to the upper-right portion of this figure, we expect that the relevant chemical potential space for our  $\text{FeWO}_4$  synthesis is closer to point C than to point A. This is consistent with observation of n- $\text{FeWO}_4$  from our synthesis as well as the observation of p- $\text{FeWO}_4$  from traditional synthesis from  $\text{FeO}$  and  $\text{WO}_3$  precursors.

## References

- (1) Suram, S. K.; Zhou, L.; Becerra-Stasiewicz, N.; Kan, K.; Jones, R. J. R.; Kendrick, B. M.; Gregoire, J. M. Combinatorial thin film composition mapping using three dimensional deposition profiles. *Review of Scientific Instruments* **2015**, *86* (3), 033904.
- (2) Mitrovic, S.; Cornell, E. W.; Marcin, M. R.; Jones, R. J. R.; Newhouse, P. F.; Suram, S. K.; Jin, J.; Gregoire, J. M. High-Throughput On-The-Fly Scanning Ultraviolet-Visible Dual-Sphere Spectrometer. *Review of Scientific Instruments* **2015**, *86* (1), 013904.
- (3) Suram, S. K.; Newhouse, P. F.; Gregoire, J. M. High Throughput Light Absorber Discovery, Part 1: An Algorithm For Automated Tauc Analysis. *ACS Combinatorial Science* **2016**, *18* (11), 673-681.
- (4) Gregoire, J. M.; Xiang, C.; Liu, X.; Marcin, M.; Jin, J. Scanning Droplet Cell for High Throughput Electrochemical and Photoelectrochemical Measurements. *Rev. Sci. Instrum.* **2013**, *84* (2), 024102.
- (5) Thimsen, E.; Martinson, A. B. F.; Elam, J. W.; Pellin, M. J. Energy Levels, Electronic Properties, and Rectification in Ultrathin p-NiO Films Synthesized by Atomic Layer Deposition. *Journal of Physical Chemistry C* **2012**, *116* (32), 16830-16840.
- (6) Hoang, K. Polaron Formation, Native Defects, and Electronic Conduction in Metal Tungstates. *Phy. Rev. Mater.* **2017**, *1* (2), 024603.
- (7) Kresse, G.; Joubert, D. From ultrasoft pseudopotentials to the projector augmented-wave method. *Physical Review B* **1999**, *59* (3), 1758-1775.
- (8) Kresse, G.; Furthmüller, J. Efficient iterative schemes for ab initio total-energy calculations using a plane-wave basis set. *Physical Review B* **1996**, *54* (16), 11169-11186.
- (9) Perdew, J. P.; Burke, K.; Ernzerhof, M. Generalized Gradient Approximation Made Simple. *Phys. Rev. Lett.* **1996**, *77*, 3865-3865.
- (10) Dudarev, S. L.; Botton, G. A.; Savrasov, S. Y.; Humphreys, C. J.; Sutton, A. P. Electron-Energy-Loss Spectra And The Structural Stability Of Nickel Oxide: An LSDA+U Study. *Physical Review B* **1998**, *57* (3), 1505-1509.
- (11) Persson, K. A. Materials Data on FeWO<sub>4</sub> (SG:13) by Materials Project. **2014**, doi:10.17188/1194432.
- (12) Jain, A.; Ong, S. P.; Hautier, G.; Chen, W.; Richards, W. D.; Dacek, S.; Cholia, S.; Gunter, D.; Skinner, D.; Ceder, G.; Persson, K. A. Commentary: The Materials Project: A Materials Genome Approach To Accelerating Materials Innovation. *Apl Materials* **2013**, *1* (1), 011002.
- (13) Ong, S. P.; Richards, W. D.; Jain, A.; Hautier, G.; Kocher, M.; Cholia, S.; Gunter, D.; Chevrier, V. L.; Persson, K. A.; Ceder, G. Python Materials Genomics (Pymatgen): A Robust, Open-Source Python Library For Materials Analysis. *Computational Materials Science* **2013**, *68*, 314-319.
- (14) Ong, S. P.; Jain, A.; Hautier, G.; Kang, B.; Ceder, G. Thermal Stabilities Of Delithiated Olivine MPO<sub>4</sub> (M = Fe, Mn) Cathodes Investigated Using First Principles Calculations. *Electrochemistry Communications* **2010**, *12* (3), 427-430.
- (15) Zhou, L.; Yan, Q. M.; Shinde, A.; Guevarra, D.; Newhouse, P. F.; Becerra-Stasiewicz, N.; Chatman, S. M.; Haber, J. A.; Neaton, J. B.; Gregoire, J. M. High Throughput Discovery of Solar Fuels Photoanodes in the CuO-V<sub>2</sub>O<sub>5</sub> System. *Adv. Energy Mater.* **2015**, *5* (22), 1500968.